A Simple System for Mapping Conductivity Microstructure

LIBE WASHBURN* AND THOMAS K. DEATON

Scripps Institution of Oceanography, La Jolla, CA 92093

(Manuscript received 18 December 1984, in final form 20 September 1985)

ABSTRACT

A system for spatial mapping of the temperature variance dissipation rate χ based on conductivity microstructure measurements from a towyo platform is described. The spatial response of the microconductivity probe is approximately that of a one-pole spatial filter with a -3 dB wavenumber of 100 cycles m^{-1}. The microconductivity system is used in conjunction with a CTD that maps the large-scale temperature, salinity and density fields along with gradient quantities such as the buoyancy frequency N. The primary use of the towyo microstructure system is the acquisition of high resolution synoptic maps of small-scale dissipative processes in relation to evolving larger scale oceanic flows.

1. Introduction

A current focus of oceanic microstructure research is the acquisition of time series at fixed locations within water masses of the vertical distribution of ϵ and χ, the rate of viscous kinetic energy dissipation and the rate of smoothing of diffusive scale temperature variance. Water masses are tagged by deploying buoys that are drogued at the depth of the water mass to be sampled. An example of persistent mixing driven by inertial wave shear in such a tagged water mass is discussed by Gregg (1984). A new observational result from this type of study is the identification of a specific large-scale flow (inertial waves in Gregg, 1984), which drives small scale turbulence processes.

A corresponding spatial analog of this research is the mapping of ϵ and χ in two (and later three) dimensions and comparing these maps with mean property distributions in an effort to identify specific large-scale features associated with small-scale mixing processes. Spatial mapping of oceanic mixing processes is not new, however, since some of the earliest microstructure measurements were obtained from two-dimensionally profiling systems (Grant et al., 1968; Nasmyth, 1972). Spatial mapping has not been pursued at the same level as vertical microstructure casts for a number of experimental reasons. A major goal of the two-dimensional measurement technique described here is the construction of synoptic maps of dissipative processes through rapidly evolving flows, such as frontal features visible in satellite images, or subsurface structures, such as salt fingering regions. Hypotheses concerning the double diffusive fluxes of heat and salt as functions of the density ratio,

$$R_\rho = \frac{\alpha}{\beta}\frac{T_z}{S_z},$$

and the buoyancy frequency,

$$N = \left(\frac{-g}{\rho}\rho_z\right)^{1/2},$$

could be examined, for example, by comparing maps of χ and ϵ with those of R_ρ and N. Here α is the coefficient of thermal expansion, β the coefficient of haline contraction, and T_z, S_z, and ρ_z the vertical gradients of temperature, salinity and density, respectively. Recent theories such as that of Gargett and Holloway (1984) regarding the functional dependence of ϵ and χ on N due to the mechanism of internal wave breaking might also be tested through spatial mapping of finestructure and microstructure quantities. Also the distribution of mixing events along isopycnal surfaces can be examined through spatial mapping of microstructure quantities.

The present paper describes a simple system for mapping conductivity microstructure, which is used for obtaining estimates of χ. Kinetic energy dissipation, while more directly interpretable in dynamical terms, is a much more difficult quantity to measure directly for a number of reasons, including motions of the instrument platform and, more fundamentally, the number of terms contributing to estimates of ϵ. With the continuing development and use of the airfoil shear probe (Crawford and Osborn, 1978; Lueck, et al., 1983), spatial mapping of ϵ should become more common. Some recent observations, Gregg (1984) and Oakey (1982), indicate that a correlation may exist be-

* Present affiliation: Center for Earth Sciences, University of Southern California, Los Angeles, CA 90089.

tween χ and ϵ that could allow interpretation of χ maps in terms of ϵ. In addition to being relatively easy to measure, values of χ can lead to estimates of vertical diffusivities, although these estimates are subject to a number of model assumptions (Gargett, 1984). As discussed by Gargett (1984), most vertical eddy diffusivity estimates to date based on direct microstructure observation result from temperature microstructure measurements (χ measurements) and rely upon models similar to that proposed by Osborn and Cox (1972). Another method for estimating the vertical eddy diffusivity of density based on measurements of ϵ is given by Osborn (1980). An additional assumption of this method is the value of a critical Richardson number that gives the ratio of buoyancy flux to turbulent production of kinetic energy.

The use of conductivity as a means of measuring temperature microstructure has been reported from a number of previous investigations including Magnell (1976) who observed salt fingers in the Mediterranean outflow and Washburn and Gibson (1984) who examined the occurrence of mixing events in the seasonal thermocline. In much of the ocean where salinity gradients are small, conductivity depends mainly on temperature and χ may be readily computed from conductivity gradient variance. However, under general oceanic conditions salinity contributions to conductivity gradient variance may not be negligible. In microstructure regions where salinity gradients are large, conductivity gradient spectra should exhibit two peaks based on the turbulent scalar mixing theory of Batchelor (1959): a low wavenumber peak due to temperature and a high wavenumber peak due to salinity. Due to the greater diffusivity of heat compared to salt ($D_T \approx 100 D_S$), the spectral peak of salinity will be about one decade higher in wavenumber than the temperature peak. Conductivity probes presently available cannot fully resolve the high wavenumber contribution due to salinity, although high wavenumber departures from the temperature portion of the conductivity spectra should be readily apparent. To estimate χ in regions of large salinity gradients, it is necessary to remove these high wavenumber contributions to conductivity gradient variance due to salinity. Despite the effects of salinity, the advantage of obtaining χ from conductivity is that high spatial resolution does not depend on low profiling speed and spatial surveys of dissipative processes in rapidly evolving flows are possible.

The microconductivity system described in this paper is used in conjunction with a Neil Brown CTD, which is itself used for producing maps of temperature, salinity and density along with gradient quantities such as N and R_ρ. Because of the much higher sampling rate required for conductivity microstructure measurement, the microconductivity signal is recorded separately from the CTD data stream. The platform described is suitable for low towing speeds only, while the microconductivity system can be deployed on much more rapidly profiling platforms and with other types of CTDs. The spatial response of the microconductivity probe has been measured in a laboratory water tunnel; these measurements are presented along with an analytical fit to the laboratory data in section 3. Details of the probe construction and microconductivity electronics are also given in section 3. Section 4 contains discussions of the alignment of CTD and microconductivity time series, the calibration procedure, and signal processing used in producing χ profiles. Data of this paper were collected during a cruise in October 1983 south of Pt. Conception along the southern California Coast.

2. Platform and experimental arrangement

The conductivity microstructure instrumentation consists of the microconductivity probe, analog conductivity electronics, pressure case, deck unit, and audio tape recorder. The pressure case and probe are mounted on a CTD which is attached to a towyo platform. A diagram of the towyo platform with CTD, microconductivity probe, and pressure case is given in Fig. 1. The CTD sensor head contains the Neil Brown conductivity cell, a platinum resistance thermometer, and a thermistor; the sensor head projects to the side at the front of the platform to reduce wake mixing effects. The platform is suspended by four cables with the front pitched up by 3 degrees, which causes the platform to be approximately level at a horizontal tow speed of 1 m s^{-1}. The four suspension cables merge about 2 m above the platform base into a clamp that attaches the entire assembly to a three conductor armored sea cable. The pitch angle was determined through tests of a half-scale model of the platform in the Scripps Hydraulics Laboratory water tunnel facility which has a 1 m^2 test section. The large fin maintains the orientation of the sensors into the flow. Due to the low platform speed the tow package is not streamlined. Depth profiling of the package is accomplished by winching through a desired depth range. Unlike more sophisticated tow platforms, which are capable of producing lift, this arrangement has minimal surface area when viewed from above to reduce pitching as the platform is moved vertically. Observation of the platform model in the water tunnel and of the full size platform at sea indicates that the assembly is well behaved at low profiling speeds. Retrieval bales facilitate deck handling of the package and a heavy probe-guard shields the microconductivity probe from the inevitable encounters with the ship's stern during deployment and retrieval.

3. Microconductivity electronics and probe

The conductivity probe, shown in Figs. 2a and 2b, and its associated electronics function as an ohmmeter measuring sea water resistivity; a current is applied

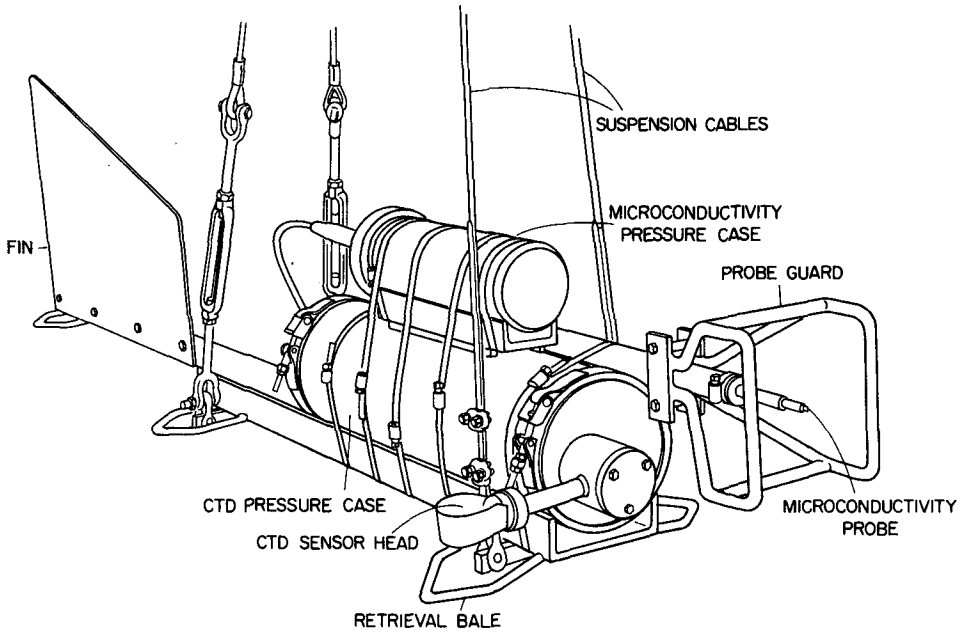

FIG. 1. Diagram of the towyo platform with microconductivity probe, pressure case and CTD. Suspension cables merge 2 m above the platform. The length of the platform is 2 m.

across a pair of electrodes immersed in the water and the resulting voltage, proportional to resistivity, is measured. Probe electrodes small enough to provide adequate spatial resolution are not likely to have an impedance that is a negligible fraction of the water resistance being measured. Furthermore, the electrode impedance may vary with time (due to removal of platinum black by surface flushing, for example). To avoid errors in the measured fluid resistivity caused by the finite electrode impedance, a second pair of electrodes was incorporated into the probe. One pair supplies a constant 4 kHz, 16 mA rms current to the water; the second pair, connected to a high impedance circuit, detects the resulting voltage drop in the water. An alternating current is used for excitation to eliminate polarization effects at the electrode surfaces. The 4 kHz sensed voltage from the second electrode pair is synchronously rectified and filtered. The filters include an LRC notch filter to remove the excitation frequency and a 3-stage RC filter to limit the signal bandwidth to 1 kHz. To reduce the dynamic range of the signal in order to simplify recording, the mean dc voltage is eliminated by high-pass filtering at 0.14 Hz. The signal is then amplified and biased to set the zero signal frequency of a voltage to frequency converter (Analog Devices AD537) to 6 kHz. The frequency modulated 6 kHz carrier is put on one conductor of the sea cable and recorded on deck on an ordinary audio tape recorder. A second conductor on the sea cable is used for transmitting the CTD data stream. On deck, in addition to being recorded, the FM carrier is demodulated and displayed in real time on a strip chart re-

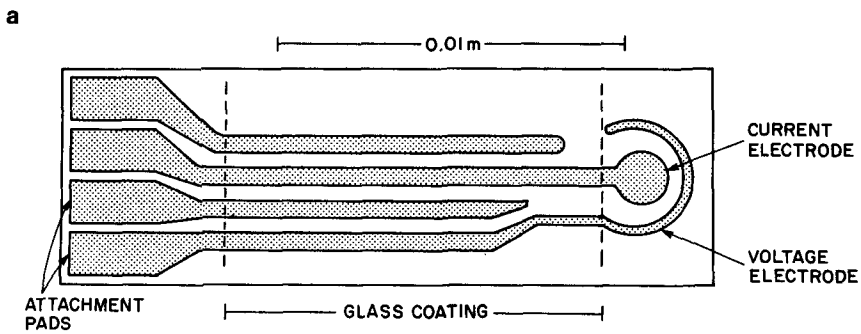

FIG. 2a. Electrode pattern on ceramic substrate. Two of the four electrodes are shown on one side of the ceramic substrate; the other two electrodes are on the opposite side of the substrate in the same pattern. Substrate thickness is about 6.4×10^{-4} m.

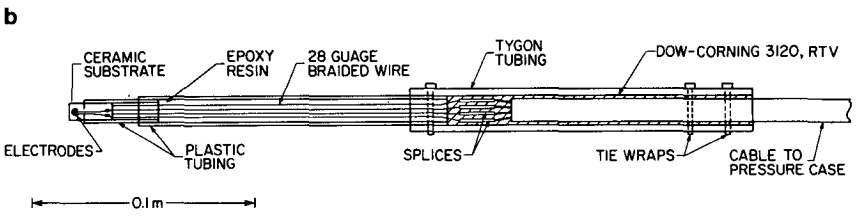

FIG. 2b. Cutaway view of the microconductivity probe assembly. The cable to the pressure case is enclosed in a hollow probe string.

corder along with a timing signal from the CTD deck unit. The overall transfer function of the microconductivity circuit, voltage to frequency converter, and deck unit demodulator electronics is flat between 0.14 and 1000 Hz. Power to the electronics package is obtained from the CTD power supply located on deck and allows microstructure sections of arbitrary length to be obtained.

The system as described above with analog recording is planned to serve as a back-up system for a fully digital recording system currently in the planning stages. Since the data of this paper were obtained in October 1983, two important additions have been made to the analog system. The recorded signal-to-noise ratio at high frequencies has been improved by prewhitening. Between 1 and 10 Hz the signal is amplified in proportion to frequency; above 10 Hz the added gain is constant at 20 dB. During playback and during real time display, a deemphasis circuit in the deck unit removes the effect of prewhitening. An improved cable driver has been added to increase the level of the FM carrier recorded on deck.

The microconductivity electrodes and ceramic substrate were designed by C. S. Cox and are shown in Fig. 2a; the other two electrodes are mounted on the opposite side of the ceramic substrate in the same configuration. All four electrodes are made of gold, which is deposited to a thickness of about 1.3×10^{-5} m. The thickness of the ceramic substrate is 6.4×10^{-4} m. As indicated in Fig. 2a, the central portion of the gold electrodes is glass coated to reduce the size of the sensing elements. The exposed portions of the electrodes to the right of the glass coating in the figure are coated with platinum black, which greatly increases the effective area of the electrodes and reduces the surface impedance.

The ceramic substrate is rigidly mounted in a pair of transparent, nesting plastic tubes that are completely filled with epoxy resin as shown in the probe assembly diagram of Fig. 2b. Two semicircular plastic bushings support the flat substrate in the round tubes. To eliminate the formation of bubbles, the epoxy resin is degassed in a vacuum chamber before the plastic tubes are filled. Braided 28-gauge wire is used to connect the electrodes to the cable that leads to the pressure case. A sleeve of Tygon tubing relieves stress on the splice between the 28-gauge wire and the cable to the pressure case and the interior of the sleeve is filled with Dow-Corning 3120 RTV, which is flexible when cured. The flexible sleeve and RTV filler compress under pressure and prevent leakage of seawater into the probe assembly. Because of the high gain in the microconductivity circuit, the cable leading to the pressure case is enclosed in a hollow probe sting to prevent flow-induced vibrations. The junction to the pressure case is made through an epoxy reinforced connector manufactured by SeaCon, Inc. The probe assembly of Fig. 2b has been tested in the laboratory to a pressure of 2000 db, but is probably suitable for use at greater pressures.

Figure 3a shows the spatial response of the microconductivity probe measured behind a grid in a water tunnel at a flow speed of 0.44 m s^{-1}. The response is obtained by computing the transfer function between signals from this probe and the conductivity probe described by Head (1983) which has a -3 dB wavenumber of about 400 cycles m^{-1}. From Fig. 3a it may be seen that the microconductivity probe used here has a -3 dB wavenumber of 100 cycles m^{-1}. The solid line in Fig. 3a is the spectral response of a one-pole spatial filter of the form $H(k)^2 = [1 + (2\pi k\tau)^2]^{-1}$, where $\tau = 0.0016$ m. This analytical form gives a reasonably good fit to the laboratory data to a wavenumber of about 500 cycles m^{-1}. Departure from the one pole response of the last two points is the result of high frequency noise in the smaller probe used for comparison in the response test.

The fitted one-pole response may be used to correct measured spectra at high wavenumbers by multiplying spectral values by the inverse of the fitted-response curve of Fig. 3a. Figure 3b shows a measured spectrum (solid line) from a region of microstructure activity out to a wavenumber of 170 cycles m^{-1} and the corrected spectrum using the one-pole response (dashed line). The original spectrum yields $\chi = 1.2 \times 10^{-5}$ C^2 s^{-1} while the corrected spectrum yields $\chi = 2.0 \times 10^{-5}$ C^2 s^{-1}, an underestimate of 40% in the original spectrum. Use of a thermistor to resolve the spectrum of Fig. 3b would require relatively large corrections for limited frequency response at high wavenumbers, even at substantially lower profiling speeds. For example, the thermistor described by Gregg et al. (1985) has a double pole filter response with a time constant of 0.006 s at a speed of 0.5 m s^{-1}. Using this relatively fast thermistor, temperature features with wavenumbers of 100

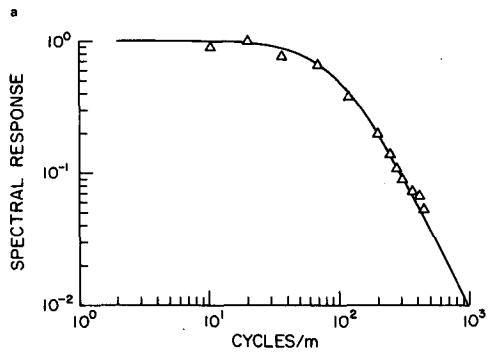

FIG. 3a. Laboratory measurement of the microconductivity probe spatial response in a water tunnel at 0.44 m s^{-1}. The solid line is the response of a 1-pole spatial filter given by $H(k)^2 = [1 + (2\pi\tau k)^2]^{-1}$, where $\tau = 0.0016$ m. The −3 dB wavenumber is 100 cycles m^{-1}.

cycles m^{-1} are attenuated by a factor of 21 at 0.5 m s^{-1}, while those at 200 cycles m^{-1} are attenuated by a factor of 231. For comparison, using the microconductivity probe described here, temperature features with wavenumbers of 100 and 200 cycles m^{-1} are attenuated by factors of 2 and 5, respectively.

The magnitude of the underestimate due to limited spatial response for a given microstructure region depends on the local kinetic energy dissipation rate ϵ in an observed microstructure region. High values of ϵ shift temperature gradient spectra to higher wavenumbers, which results in greater attenuation of measured spectral levels in the portion of the spectrum that dominates the variance. As shown by Dillon and Caldwell (1980) and Oakey (1982), the high wavenumber range of oceanic temperature gradient spectra is in reasonable agreement with the theory of Batchelor (1959). Using the theoretical spectral form of Batchelor (1959) given by Dillon and Caldwell (1980), and assuming the laboratory-derived one-pole spatial response of this probe with $\tau = 0.0016$ m, the fraction of χ resolved without correction may be estimated for the range of ϵ typically encountered in the ocean. Figure 3c gives the fraction of variance resolved as a function of ϵ for ϵ in the range 10^{-11} to 10^{-5} W kg^{-1}. From the curve of Fig. 3c it may be seen that more than half of χ is resolved without correction for $\epsilon \leq 4 \times 10^{-7}$ W kg^{-1}. Application of the spatial response correction allows χ to be estimated throughout the range of ϵ encountered in the ocean.

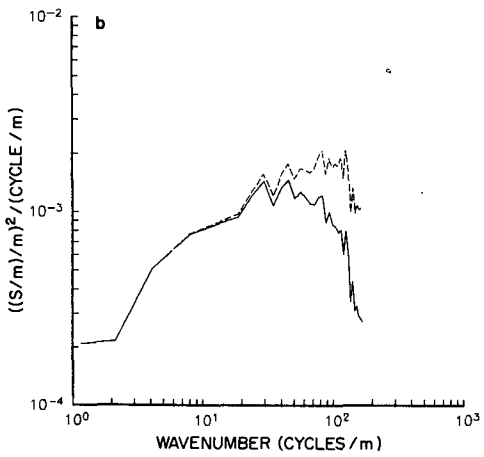

FIG. 3b. Comparison of conductivity gradient spectra before correction for limited spatial resolution (solid line) and after correction using the inverse of the fitted one-pole response of Fig. 3a (dotted line).

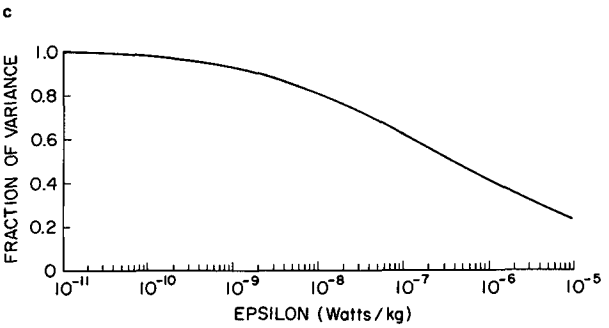

FIG. 3c. Fraction of χ resolved as a function of kinetic energy dissipation rate ϵ.

Figure 4 contains two sequential upcast and downcast pairs of analog microconductivity traces recorded at sea. In each panel the left trace is the recorded signal and the right trace is identical but high pass-filtered at 1 Hz and amplified by a factor of 2 to emphasize high frequency activity. The upper frequency limit of the strip chart recorder used for producing the traces in Fig. 4 is about 100 Hz and wavelengths contributing to the right-hand traces in each panel range from about 1.4–0.014 m. Solid lines running among the traces delineate regions of strong microstructure activity encountered repeatedly on upcasts and downcasts. Several finestructure features with vertical scales of 2–5 m may also be traced among the profiles. Since the traces of Fig. 4 are time based, variations in platform speed cause constant pressures to be shifted vertically from trace to trace.

4. Calibration and data processing

Because the microconductivity data stream is recorded separately, it must be synchronized with the CTD data stream during subsequent analysis. To do this a voltage ramp that varies from 0 to 5 volts is generated through digital to analog conversion of a counter in the CTD deck unit. The ramp resets every 256 s as measured by a clock in the CTD and is used for aligning the microconductivity and CTD time series through software. This ramp is converted to an FM signal centered at 6 kHz which is recorded at the same time as the microconductivity signal. For the data of this paper the microconductivity signal was sampled at 512 Hz, 16 times the digitization rate of individual

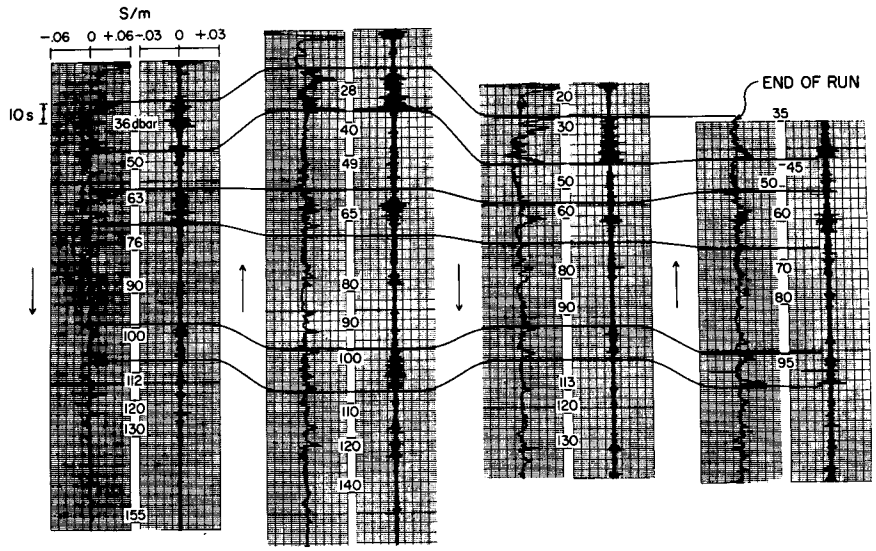

FIG. 4. Analog microconductivity traces recorded at sea showing regions of strong microstructure activity encountered repeatedly on upcasts and downcasts. The right-hand trace of each panel has been high-pass filtered at 1 Hz and amplified by a factor of 2. Arrows indicate the direction of travel and depths are marked at the center of each panel.

CTD sensors, which provides a point about every 3 mm along the towpath. Normally the microconductivity signal is subsampled or some time-averaged statistic (such as χ) computed and stored in a disc file along with the CTD time which has been converted from the analog time ramp. Merging of the data series is done through linear interpolation between CTD and microconductivity data files based on CTD time. Alignment of the CTD and microconductivity time series is critical to the calibration procedure described below. Misalignment in time between the two time series increases scatter in the calibration plot (Fig. 5b)

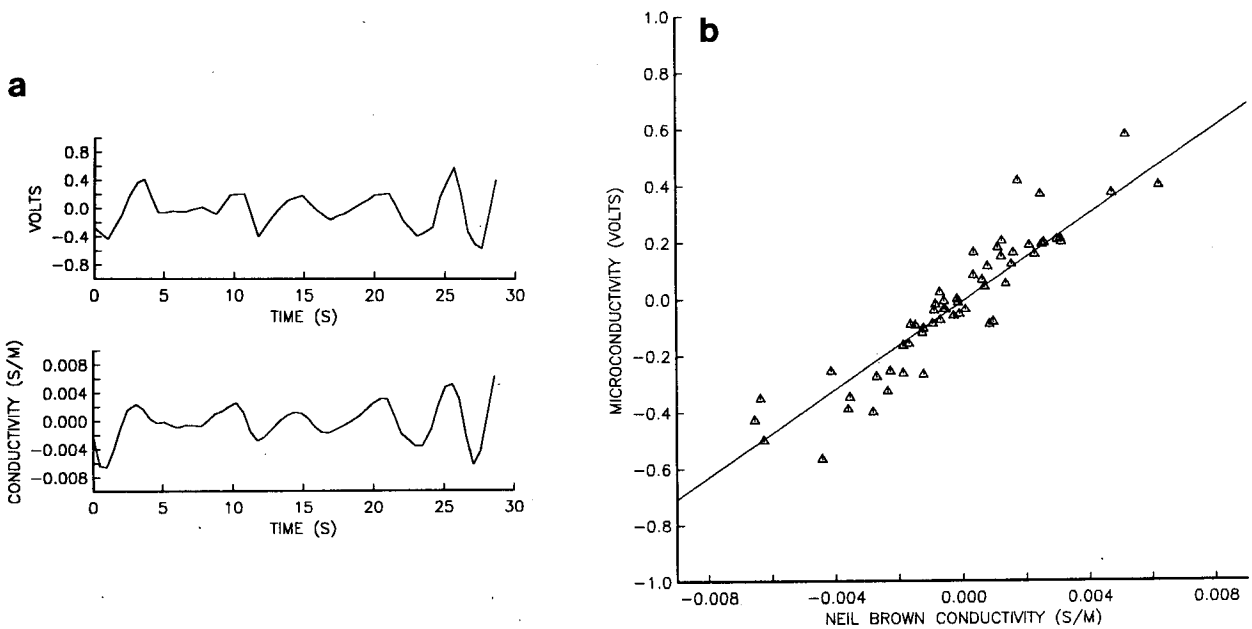

FIG. 5. (a) Time series of microconductivity signal in V (upper plot) and Neil Brown conductivity signal in S m^{-1} (lower plot), (b) Scatter plot and least-squares fit for the data of Fig. 5a.

and reduces the reliability of the least square fit used for obtaining the calibration factor. For 1 s averaged or subsampled quantities, spatial alignment between the CTD and microconductivity time series is less than 0.5 m.

The microconductivity signal is calibrated by comparison with the signal from the Neil Brown conductivity cell. In the calibration procedure both signals are digitally band-pass filtered for a range of frequencies that are resolved by both probes. The lower frequency limit is set by the analog high pass filter in the microconductivity electronics and the upper limit is chosen to smooth both time series and avoid aliasing effects due to undersampling in the Neil Brown conductivity cell. The lower frequency limit of the filtering band is more critical to the calibration procedure because the low frequency conductivity spectrum is red with spectral slope in the range -2 to -3 and thus, low frequency contributions dominate the conductivity variance in the filtering band. The red conductivity spectrum is due to temperature finestructure on vertical scales of 1 m and larger. A 55-weight finite impulse response digital filter with -3 dB frequency corresponding to 0.14 Hz and stop band attenuation of -100 dB is used for high pass filtering of both signals. A 1 s running mean filter ($f_{-3\,\mathrm{dB}} = 0.44$ Hz) is used for low pass filtering of the signals. An example of this digital filtering procedure is shown in Fig. 5a for 28 s time series of the band-passed microconductivity signal in volts (upper plot) and Neil Brown conductivity signal in S m^{-1} (lower plot). The calibration factor is determined from a least square fit to a scatter plot of Fig. 5a; this scatter plot and the least square fit (correlation coefficient is 0.92) with a calibration factor of 0.013 S m^{-1} V^{-1} are shown in Fig. 5b. While this calibration procedure is somewhat crude compared to more standard laboratory procedures, it has the advantage of permitting calibration checks at any point in the data record. It should be emphasized that relative levels of activity among microstructure regions are not affected by calibration errors.

Values of χ are estimated as

$$\chi = 6D\left(\frac{\partial\sigma}{\partial T}\right)^{-2}_{S,P}\left(\frac{d\sigma}{dx}\right)^2,$$

where σ is conductivity, D is the thermal diffusivity of sea water and x is displacement along the measurement path. This estimate assumes isotropy at small scales and that the conductivity gradients are due mainly to temperature which is true for the data presented in this paper. Spatial gradients are computed from temporal gradients by using the Taylor hypothesis of frozen flow according to the relation $d/dx = (U^2 + W^2)^{-1/2}d/dt$, where W and U are the vertical and horizontal components of the platform velocity with respect to the water. On average, the platform speed is about 1.45 m s^{-1} for these data. Instantaneous vertical velocity W as a function of time used in estimating χ is computed by differencing half-overlapped, 1 s averages of the pressure signal and assuming 1 db to be 1 m. Typical average vertical velocities of the package on both upcasts and downcasts are about 0.6 m s^{-1}. Examples of 1 s averages of the CTD pressure signal and its first difference dP/dt are given in Fig. 6 along with the CTD thermistor signal in the bottom time series. Ideally the platform would be moved vertically at a constant speed, however, due to heaving of the towing vessel by surface waves, the vertical velocity of the package is constantly changing as may be seen in the plot of dP/dt in Fig. 6. Superimposed on the mean vertical velocity is a nearly sinusoidal velocity variation with an amplitude of about 0.3 m s^{-1} with 6–8 s period. The observed first difference values of Fig. 6 are typically much greater than the least count of 0.025 db for the pressure transducer. Estimates of χ are computed over 1 s time in-

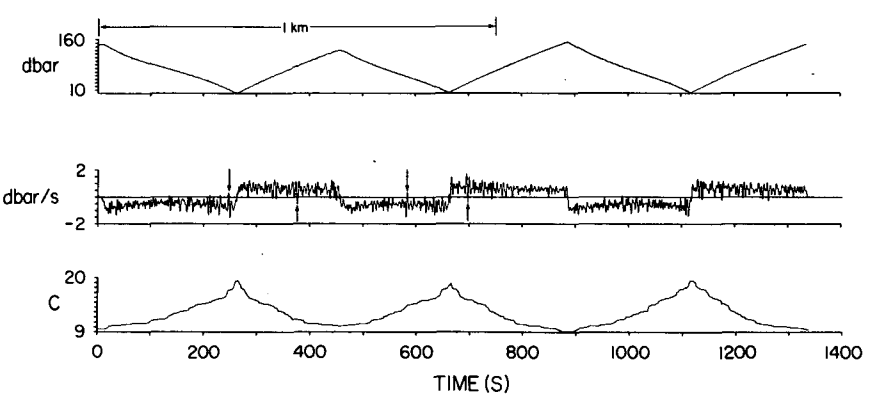

FIG. 6. Time series of pressure (upper plot); first difference of pressure (center plot), which is used for estimating vertical velocity; and CTD thermistor temperature (lower plot) covering a horizontal distance of approximately 1700 m. Arrows indicate direction reversals in the pressure difference time series.

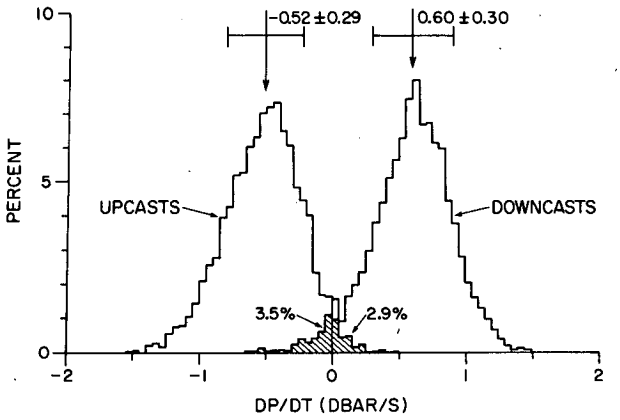

FIG. 7. Histograms of the first difference of pressure for a 6900 m record separated into upcasts and downcasts. Hatched area identifies fractions of record containing direction reversals.

tervals to minimize smearing in wavenumber due to this variation in the platform speed, although some smearing is unavoidable. Vertical velocity reversals (indicated by arrows) during both upcasts and downcasts are evident at a few places in the dP/dt time series of Fig. 6. Histograms of dP/dt computed for 12 upcast, downcast pairs from a total record length of 1.6 hours are shown in Fig. 7 and reveal that these reversals occur about 3.5% of the time on downcasts and 2.9% of the time on upcasts as indicated by the hatched areas. Also shown in Fig. 7 are the mean pressure derivatives and bars indicating plus and minus one standard deviation in dP/dt.

The horizontal component of the package velocity U is estimated from 15 min averages of position by using Loran-C fixes. For the data reported here the average horizontal velocity over ground is 1.32 ± 0.09 m s^{-1}. Because this estimate is obtained over land, local currents will result in velocity errors that depend on current magnitude, direction, and ship heading. For example, a current velocity of 0.2 m s^{-1} opposite the direction of tow results in a systematic 25% underestimate of χ for the horizontal, overland velocity of 1.32 m s^{-1} of these data.

In the absence of local currents, use of Loran-C fixes to estimate U results in a systematic error in χ estimates between upcasts and downcasts. On upcasts the estimated horizontal velocity will be less than U because, in addition to being moved vertically, the platform is moved horizontally toward the towing vessel. Since the platform speed is underestimated on upcasts and since χ depends on the inverse square of platform speed, estimated χ values will exceed the actual values. Similarly, on downcasts the horizontal platform speed is less than U because the platform moves horizontally away from the towing vessel and χ is underestimated. For these data the average value of $(d\sigma/dt)^2$, from which $(d\sigma/dx)^2$ is computed, on upcasts exceeds that of downcasts by a factor of 1.78 and is consistent with an average horizontal platform speed on upcasts of 1.6 m s^{-1} and on downcasts of 1.1 m s^{-1}. In terms of χ, on average upcast χ values are about 25% too large while on downcasts they are about 25% too small. The instantaneous horizontal speed, which is unknown, is different from the average values and represents a source of random error in estimating χ. Also, as a consequence of the differing average velocities, the average towing angle with respect to the horizontal is different between upcasts and downcasts: here, the upcast towing angle is about 18° and the downcast angle is about 29°.

Examples of two χ profiles versus depth are given in the center panels of Figs. 8 and 9. The corresponding temperature signal from the CTD is shown in the left-hand panel; the microconductivity signal is plotted in the right-hand panel. The microconductivity signal on the downcast shown in Fig. 8 contains large, negative conductivity excursions due to steps in the temperature profile. The high pass filtering in the microconductivity electronics results in the temperature steps appearing as local minima in the conductivity record of Fig. 8. On the following upcast (shown in Fig. 9), the microconductivity excursions are reversed as warmer, more conductive water is encountered. A region of strong microstructure activity with χ exceeding 2×10^{-5} C^2 s^{-1} at a few points is seen in both the downcast and upcast χ profiles of Figs. 8 and 9 between 40 and 60 db. Because the data are recorded along a sloping tow-path, midpoints of adjacent profiles are separated horizontally by about 300 m and the mixing region between 40 and 60 db in Figs. 8 and 9 has a horizontal extent of at least 450 m. The upper limit of both profiles is at the high gradient region at the base of the surface mixed layer, which extends down to about 16 db. The

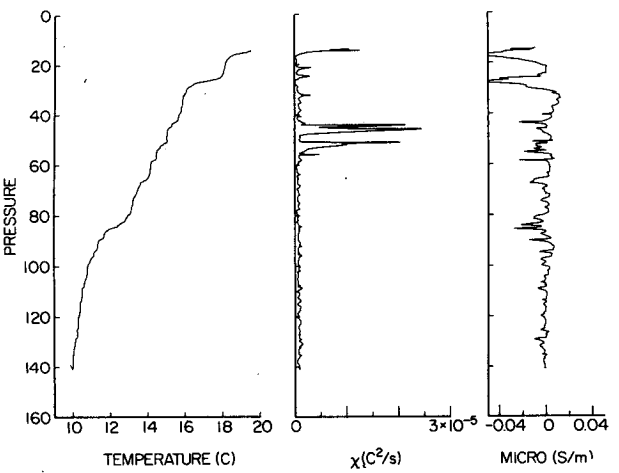

FIG. 8. From left to right: temperature profile from the CTD, χ profile derived from the microconductivity signal, and the microconductivity signal. All profiles recorded on a downcast.

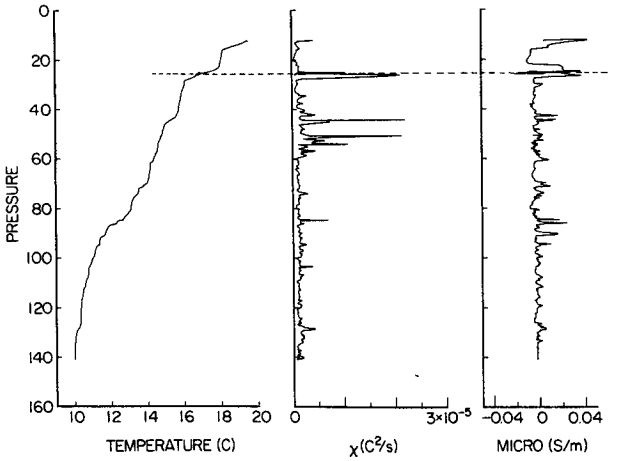

FIG. 9. As in Fig. 8, but for an upcast. Dashed line marks depth where winching was stopped for several seconds, but horizontal towing maintained.

dashed line at 26 db in Fig. 9 indicates a position in the profile where vertical winching was stopped for several seconds, but horizontal towing maintained. Irregularities appear in all three profiles of Fig. 9 at this depth due to repeated profiling from ship heave over a depth range of 0.6 m.

Figure 10 shows a comparison between a conductivity gradient spectrum from a region of strong microstructure activity ($\chi = 1.3 \times 10^{-5}$ C^2 s^{-1}) and noise spectra recorded and on a downcast (solid line) and upcast (dashed line). All three spectra are computed from 20 s time series or about 30 m along the towpath. Generally the signal spectral levels are about 2 orders of magnitude above the noise level. Greater signal-to-noise ratio is achieved for the 1 s averages normally computed for mapping χ.

A few narrow-band noise peaks may be seen in the spectra; a large peak at 40 Hz is clearly evident in the upcast noise spectrum and in the signal spectrum which is also from an upcast. A second harmonic at 80 Hz is visible in the upcast noise spectrum. A much smaller peak occurs at about 30 Hz in the downcast spectrum, but is not evident in the upcast noise spectrum. These peaks at 30 and 40 Hz may be the result of vortex shedding from the towing cable. The Reynolds number of the cable, which has a diameter D of 0.0074 m, is about 10^4 at the average horizontal towing speed $\bar{U}$ of 1.32 m s^{-1}. Using laboratory data for flow around cylinders of Fung (1969), the nondimensional vortex shedding frequency is given by the Strouhal number St and is in the range 1.15 to 1.25 for this Reynolds number. The dimensional shedding frequency f is expressed as

$$f = \frac{\mathrm{St}}{2\pi}\left(\frac{\bar{U}}{D}\right),$$

and for the range of St given above predicts shedding in the frequency range 40 to 43 Hz for the upcast $\bar{U}$ of 1.6 m s^{-1} and 27 to 30 Hz for the downcast $\bar{U}$ of 1.1 m s^{-1}. The observed peaks fall within these ranges and the much greater amplitude of the upcast peak may result from the higher flow velocity past the towing cable. The effect of the large peak during upcasts is evident in the χ profiles where the noise level is somewhat larger during the upcast in Fig. 9 compared to the downcast in Fig. 8. Addition of a fairing to the sea cable should greatly reduce this effect.

Because noise spectral levels shown in Fig. 10 increase with frequency, the effective noise level of χ is a strong function of the upper limit of integration used for estimating conductivity gradient variance. Typical temperature microstructure signal spectra, on the other hand, reach a maximum and then decrease with frequency as may be seen in the upper spectrum of Fig. 10. Values of χ shown in Figs. 8 and 9 include variance contributions to 250 Hz, which corresponds to wavenumbers of about 200 cycles m^{-1} in order to resolve the maximum χ levels present. Inclusion of variance to 250 Hz results in a noise χ of about 9.7×10^{-7} C^2 s^{-1} at the average platform speed of 1.45 m s^{-1}. This noise level is due to the limited signal to noise ratio (about 44 dB) of the audio tape recorder used for recording the 6 kHz carrier. The noise level measured

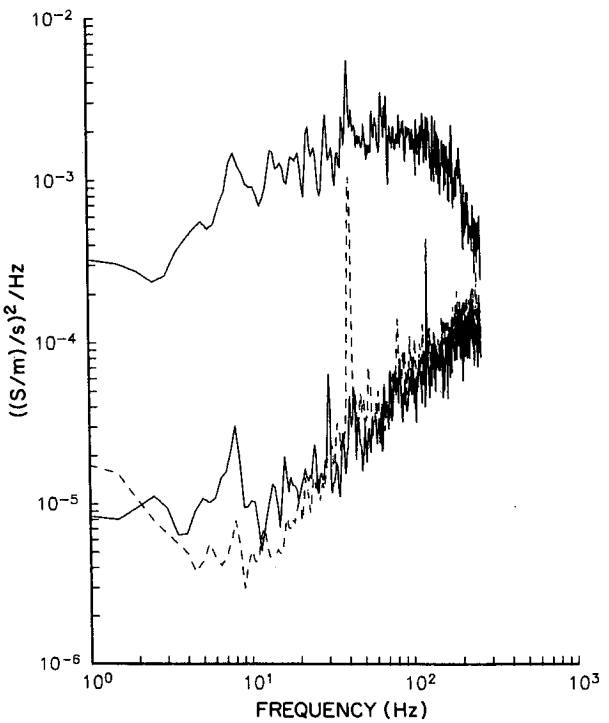

FIG. 10. Signal spectrum (upper curve) from a region of microstructure activity compared to noise spectra (lower curves) recorded on a downcast (solid curve) and upcast (dashed curve).

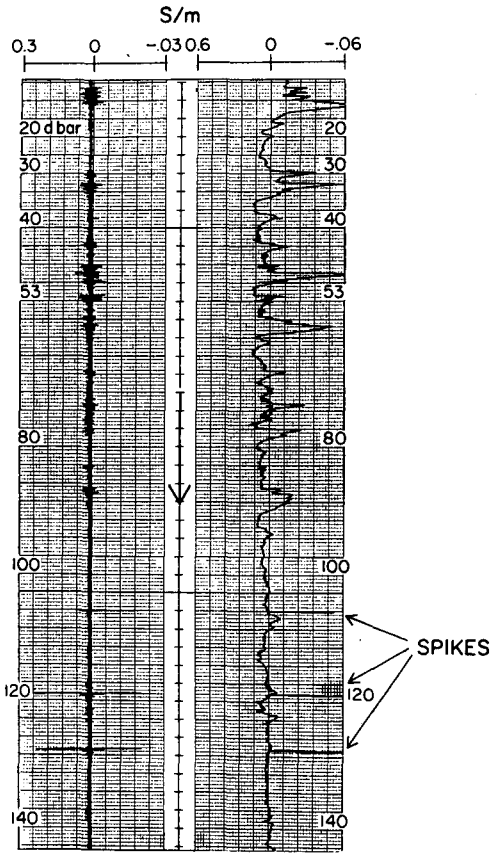

FIG. 11. Analog conductivity record from a downcast showing three spikes, all toward lower conductivity, which may be the result of collisions with biological material.

in the laboratory that results from the tape recorder is within 10% of the observed noise level at sea. Addition of the prewhitening circuit since the data of this paper were taken increases the signal to noise ratio during audio recording by about 20 dB. Direct digitization of the microconductivity signal at sea will eliminate effects of tape recorder noise entirely.

Some spikes were encountered in the microconductivity time series and are believed to be the result of impacts with biological material. The sign of the spiking is consistently negative (lower conductivity) on both upcasts and downcasts. The spikes also tend to occur in groups. An example of three spikes recorded on an analog trace during a downcast is shown in Fig. 11. Similar spikes which are usually negative have also been observed in other investigations employing small scale conductivity measurements (Okawa and Dugan, 1984).

5. Discussion

A simple system for spatial mapping χ based on conductivity microstructure measurements is described and consists of a microconductivity probe, analog electronics, pressure case, deck unit and audio tape recorder. The system is used in conjunction with a CTD, which maps the large scale temperature, salinity, and density fields along with gradient quantities such as the buoyancy frequency N. The microconductivity probe spatial response is that of a one-pole spatial filter with a -3 dB wavelength of 1 cm. The spatial response is adequate to resolve χ for the range of kinetic energy dissipation rate typically encountered in the ocean. Calibration of the microconductivity probe is done by comparison with a digitally filtered version of the CTD conductivity signal. While the tow platform described here is suitable only for low speed operation (1–2 m s^{-1}), the microconductivity system is adaptable to other, higher performance instrument platforms. The recording method employing an audio tape recorder is intended to serve as a backup system for direct digitizing of data at sea.

Acknowledgments. Libe Washburn would like to thank Charles S. Cox for generous use of laboratory facilities during the development of this instrument. Laurence Armi provided helpful advice and encouragement throughout the project. Sharon Yamasaki and Pierre Flament developed much of the software for processing the CTD towyo data. Mark Baker is largely responsible for the laboratory measurement of the spatial response of the microconductivity probe. Helpful discussions were had with Timothy F. Duda and Carl H. Gibson. Walter Richter gave valuable assistance at sea during the experiment in which these data were collected. Thanks also to Timothy Boyd, Richard Williams, William Watkins and Vittorio Barale who assisted in the data collection. Richard Olsen assisted in subsequent development, construction, and testing of the electronics. Finally, we would like to acknowledge the helpful support of Captain Tom Beattie and the crew of the *Ellen B. Scripps* throughout the experiment. This work was supported by the Office of Naval Research, Contract USN-N00014-80-C-0440.

REFERENCES

Batchelor, G. K., 1959: Small scale variation of convected quantities like temperature in turbulent fluid. *J. Fluid Mech.*, **5**, 113–133.

Crawford, W. R., and T. R. Osborn, 1978: Microstructure measurements in the equatorial Atlantic during GATE. *Deep Sea Res.*, **26**, (GATE Suppl. II), 285–308.

Dillon, T. M., and D. R. Caldwell, 1980: The Batchelor spectrum and dissipation in the upper ocean. *J. Geophys. Res.*, **85**, 1910–1916.

Fung, Y. C., 1969: *Introduction to Aeroelasticity,* Dover, 498 pp.

Gargett, A. E., 1984: Vertical eddy diffusivity in the ocean interior. *J. Mar. Res.*, **42**, 359–393.

——, and G. Holloway, 1984: Dissipation and diffusion by internal wave breaking. *J. Mar. Res.*, **42**, 15–27.

Grant, H. L., A. Molliet and W. M. Voget, 1968: Some observations of turbulence in and above the thermocline. *Fluid Mech., Vol. 34* (3), 443–448.

Gregg, M. C., 1984: Persistent turbulent mixing and near-inertial waves. *Proc. of the Second 'Aha Huliko a'Hawaiian Winter Workshop,* City, Office of Naval Res., Manoa, 299 pp.

——, E. A. D'Asaro, T. J. Shay and N. Larson, 1986: Observations of persistent mixing and near-inertial waves. *J. Phys. Oceanogr.,* **16,** 856–885.

Head, M. J., 1983: The use of miniature four-electrode conductivity probes for high resolution measurement of turbulent density or temperature variations in salt-stratified water flows. Ph.D. thesis, University of California, San Diego, 211 pp.

Lueck, R. G., W. R. Crawford and T. R. Osborn, 1983: Turbulent dissipation over the continental slope off Vancouver Island. *J. Phys. Oceanogr.,* **13,** 1809–1818.

Magnell, B., 1976: Salt fingers observed in the Mediterranean outflow region (34°N, 11°W) using a towed sensor. *J. Phys. Oceanogr.,* **6,** 511–523.

Nasmyth, P. W., 1972: Oceanic turbulence. Ph.D. thesis, University of British Columbia, 69 pp.

Oakey, N. S. 1982: Determination of the rate of dissipation of turbulent energy from simultaneous temperature and velocity sear microstructure measurements. *J. Phys. Oceanogr.,* **12,** 256–271.

Okawa, B. S., and J. P. Dugan, 1984: Contamination of conductivity measurements by waterborne particles, *Ocean Eng.,* **11**(3), 265–279.

Osborn, T. R., 1980: Estimates of the local rate of vertical diffusion from dissipation measurements. *J. Phys. Oceanogr.,* **10,** 83–89.

——, and C. S. Cox, 1972: Oceanic fine structure. *Geophys. Fluid Dyn.,* **3,** 32–345.

Washburn, L., and C. H. Gibson, 1984: Horizontal variability of temperature microstructure at the base of a mixed layer during MILE. *J. Geophys. Res.,* **89**(C3), 3507–3522.